Versatile, modular 3D microelectrode arrays for neuronal ensemble recordings: from design to fabrication, assembly, and functional validation in non-human primates

2017 J. Neural Eng. 14 036010

(http://iopscience.iop.org/1741-2552/14/3/036010)

IOP Publishing Journal of Neural Engineering
J. Neural Eng. **14** (2017) 036010 (16pp) https://doi.org/10.1088/1741-2552/aa5a90

Versatile, modular 3D microelectrode arrays for neuronal ensemble recordings: from design to fabrication, assembly, and functional validation in non-human primates

F Barz[1,2], A Livi[3], M Lanzilotto[3], M Maranesi[4], L Bonini[4], O Paul[1,2] and P Ruther[1,2]

[1] Department of Microsystems Engineering (IMTEK), University of Freiburg, Freiburg, Germany
[2] BrainLinks-Brain Tools, University of Freiburg, Freiburg, Germany
[3] Dipartimento di Neuroscienze, Università degli Studi di Parma, Parma, Italy
[4] Istituto Italiano di Tecnologia (IIT), Brain Center for Social and Motor Cognition, Parma, Italy
E-mail: falk.barz@imtek.uni-freiburg.de

Received 27 September 2016, revised 10 January 2017
Accepted for publication 11 January 2017
Published 29 March 2017

Abstract

Objective. Application-specific designs of electrode arrays offer an improved effectiveness for providing access to targeted brain regions in neuroscientific research and brain machine interfaces. The simultaneous and stable recording of neuronal ensembles is the main goal in the design of advanced neural interfaces. Here, we describe the development and assembly of highly customizable 3D microelectrode arrays and demonstrate their recording performance in chronic applications in non-human primates. *Approach.* System assembly relies on a microfabricated stacking component that is combined with Michigan-style silicon-based electrode arrays interfacing highly flexible polyimide cables. Based on the novel stacking component, the lead time for implementing prototypes with altered electrode pitches is minimal. Once the fabrication and assembly accuracy of the stacked probes have been characterized, their recording performance is assessed during *in vivo* chronic experiments in awake rhesus macaques (Macaca mulatta) trained to execute reaching-grasping motor tasks. *Main results.* Using a single set of fabrication tools, we implemented three variants of the stacking component for electrode distances of 250, 300 and 350 μm in the stacking direction. We assembled neural probes with up to 96 channels and an electrode density of 98 electrodes mm^{-2}. Furthermore, we demonstrate that the shank alignment is accurate to a few μm at an angular alignment better than 1°. Three 64-channel probes were chronically implanted in two monkeys providing single-unit activity on more than 60% of all channels and excellent recording stability. Histological tissue sections, obtained 52 d after implantation from one of the monkeys, showed minimal tissue damage, in accordance with the high quality and stability of the recorded neural activity. *Significance.* The versatility of our fabrication and assembly approach should significantly support the development of ideal interface geometries for a broad spectrum of applications. With the demonstrated performance, these probes are suitable for both semi-chronic and chronic applications.

Keywords: 3D microelectrode array, intracortical neural probe, brain–machine interface, microelectromechanical systems, chronic neural recording in macaques, single-unit activity, reaching-grasping

(Some figures may appear in colour only in the online journal)

1. Introduction

Intracortical, multichannel neural recording capable of resolving neuronal activity at the single-unit (SUA) and multi-unit (MUA) level is a fundamental tool in neuroscientific research. In addition, it is crucial for the development of neural prostheses targeting the restoration of sensory and motor functions [1]. Indeed, MUA and SUA yield the most detailed information for decoding control parameters required for brain–machine interfaces. However, this being critically connected to the number of units that can be simultaneously recorded [2]. Their stable isolation over time is definitely a further requirement.

The Utah electrode array (UEA) is one of the first tools developed for this purpose [3–7]. The array has been used in the peripheral as well as central nervous system (CNS) in animal experiments and human trials, with stable SUA exceeding one year [8]. Recently, a UEA-based neural bypass system was demonstrated to alleviate the effect of a spinal cord injury on the upper limb motor control in a human [9]. Despite its success, the UEA has the limit of being based on a 10×10 array of short silicon (Si) microneedles, with a single recording site at the end of each shank. A first step towards an increased number of electrodes per probe shank was recently proposed [10]. Nevertheless, because of the applied fabrication process, the shank lengths of the UEA are typically limited to 2 mm, which makes it difficult to access deeper cortical structures.

Multisite Si-based neural probes constitute an alternative to overcome these limits, since they provide optimal recording quality with a strongly increased number of channels per tissue volume at minimum system dimensions. Indeed, established standard fabrication processes from microelectronics and microsystems technology enable recording systems with two-dimensional (2D) and three-dimensional (3D) microelectrode arrangements [11, 12]. Some of them can be used in a floating manner, decoupled from the skull to increase the stability of acute neural recordings [13]. The majority of the 3D electrode arrays relies on the planar, Michigan-style probes [14] that have been assembled into compact probe arrays [15–25]. The planar microelectrode arrays can comprise multiple probe shanks with electrodes made from various electrode materials freely positioned along shank lengths of up to several millimeters. Their assembly into 3D electrode arrays then provides additional degrees of freedom to create customized recording solutions. Compared to the concept of the Utah array, this approach represents a more flexible answer to the often formulated request for customizability of probes to specific brain regions targeted in research and neuroprosthetic application [8, 12, 21, 26]. The majority of such probes either employs a common Si platform to accommodate the electrode arrays or uses a stacking approach for system assembly. The advantages and disadvantages of these two approaches are now briefly discussed before we introduce our flexible, modular design.

Platform-based 3D electrode arrays have generally comprised a common platform with a thickness of a few 100 μm from which probe combs orthogonally project into the targeted neural tissue [15–20]. The platform is used to bundle the signal lines from individual planar electrode arrays with the purpose of interfacing them with external instrumentation. The transfer of the wiring from the electrode arrays to the platform presents a delicate assembly step of this kind of probes and has been the central topic of several technical studies. The proposed solutions have made use of mechanical interconnecting [15–18], electroplating [19] and soldering techniques [20] to close the gap between the wiring on the platform and probe combs. Despite the technical challenges, the resulting 3D probes are highly compact and often require only a single cable for electrical interfacing, which simplifies device handling [17]. On the other hand, the platform approach is rather unfavorable with regards to probe customizability. In fact, the slots or recesses commonly used to position the Michigan-style probes within the platform are reserved for components with a specific channel count. Neither can the channel count nor the position of a probe within the platform be changed after platform fabrication and for a given set of tools, i.e. photolithography masks used to define the electrical wiring on the platform and the probe position within it. Customization of these probes is thus always accompanied by a significant temporal and monetary overhead.

Merriam *et al* and later NeuroNexus (Ann Arbor, MI, USA), presented a technical solution to this issue of design inflexibility by reducing the platform functionality to the alignment, orientation and fixation of planar probes [21, 22]. In this modified platform approach, individual planar probes interface directly with highly flexible ribbon cables. A transfer of the electrical wiring is thus not required after the probes have been inserted into the common platform. The approach thereby decouples the channel count of the planar probes from the platform design and increases the design freedom. Nevertheless, even in this concept, changing the distance between individual probes is possible only by modifying the mask layout for platform fabrication.

Stacked probes on the other hand offer the largest design freedom among the 3D electrode arrays assembled from Michigan-style probes. This assembly scheme stacks planar probes at a predefined vertical separation followed by adhesive bonding. The exact and parallel probe alignment represents a critical aspect of the often manual assembly of this array variant. In the simplest form, two planar probes interfaced by flexible cables are adhesively bonded to each other back-to-back [23]. However, the stacking sequence is in this case limited to a pair of probes. In addition, the probe spacing is not customized easily nor is the shank alignment highly reproducible due to the manual assembly.

An efficient assembly technique based on an anisotropically conducting film (ACF) serving as an adhesive layer between flexible printed circuit boards (fPCBs) and Si-based electrode arrays has been introduced by Du *et al* [24]. The ACF film enables the electrical interfacing between the probes and the fPCBs. The thickness of the three components defines the vertical probe separation in the stacked array. In principle, each component of this 3D array can be modified and exchanged independently. Furthermore, the channel count of the stacked array can be freely increased within practical limits. Probe alignment within the array is a critical aspect since the assembly has been again carried out manually.

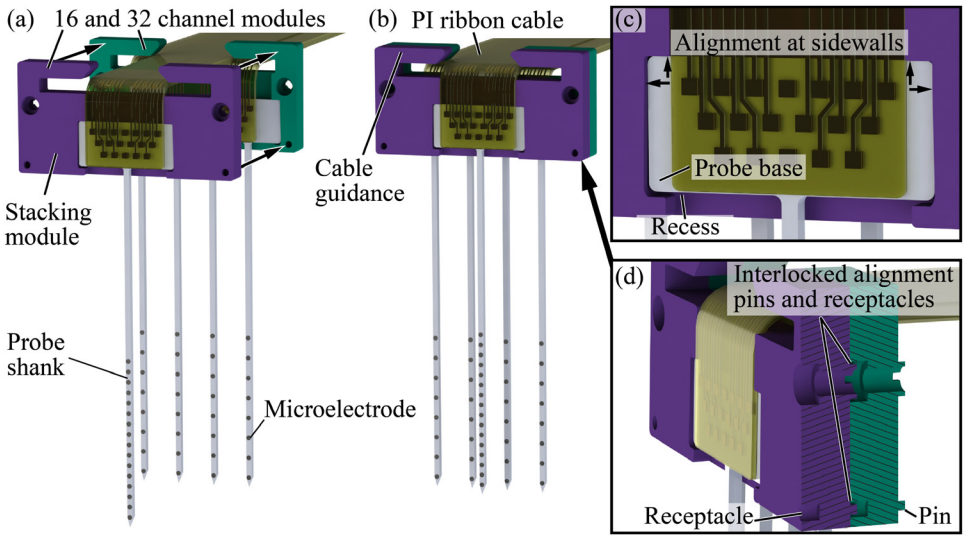

Figure 1. Schematic of (a) two SEAs composed of a single-shank and a four-shank probe, respectively, interfacing PI cables and (b) combination of the SEAs forming a 48-channel 3D electrode array. (c) Stacking module features implemented for probe base alignment within the module and (d) cross-section of a stacked array indicating interlocking alignment pins on the rear and shallow recesses on the front of the stacking modules for the alignment of SEAs.

The stacking approach by Chang *et al* addresses the probe alignment by using dedicated electrode arrays and spacer components both fabricated from Si and accurately combined with each other using a flip-chip bonder [25]. The resulting probe exhibits a cascaded structure at its distal end that is crucial for the electrical interconnection of this array to a printed circuit board by a serial wire bonding process. Compared to the approach of Du *et al*, the design freedom is definitely reduced as each probe comb is designed for a specific layer within the stacked probe. Furthermore, wire bonding and the probe base length represent practical constraints for the probe assembly. The rigid connection between electrodes and PCB might further limit the application of these probes to acute experiments.

In contrast to these approaches, we present a fabrication and assembly concept that combines the advantages of scalability and compactness of the assembly with an electrode alignment accurate within a few μm. The approach relies on a novel micromachined stacking component that allows to position planar microelectrodes freely in a 3D configuration. The stacking period within the probe combs can be adapted over a range of several hundred micrometers without the need to modify any fabrication tool. Besides the characterization of fabrication and assembly tolerances, this study presents the excellent single-unit recording capability of these probes in behavioral experiments in non-human primates (NHP). The recording success is supported by a low tissue reaction to the implanted probes evidenced by histology results obtained with one of the recorded animals.

2. Materials and methods

2.1. 3D electrode array design

The key components of the 3D electrode arrays developed in this study are micromachined stacking modules that allow to extend an existing portfolio of planar probes into complex arrangements in a flexible and accurate manner. As illustrated in figure 1(a), planar, Michigan-style probes interfacing highly flexible, 10-μm-thin polyimide (PI) cables are positioned in the stacking module to form a so-called stackable electrode array (SEA). Multiple SEAs are then stacked to form the 3D electrode array, as depicted in figure 1(b). The planar electrode arrays used here may feature a single probe shank or multiple shanks connected to a common probe base (figures 1(a) and (b)). Along the individual probe shanks, the intended number of microelectrodes is distributed at the desired longitudinal and lateral pitch. The PI ribbon cables used to interface the electrode arrays with an external instrumentation are flip-chip (FC) bonded to the probe base, as detailed elsewhere [27].

The stacking modules feature so-called cable guidances that orthogonally redirect the cable from the various stacking planes and collect them into a cable bundle. This feature facilitates probe handling and also reduces the elevation of the system above the cortical tissue.

The accurate and highly parallel alignment of the probe shafts both in-plane and out-of-plane is due to dedicated alignment features integrated in the stacking modules. The lateral and angular alignment of the probe base relative to the stacking module is guaranteed by the deep recess in the module destined to host the probe base, as shown in figure 1(c) and in further detail in figure 2. It exhibits a lateral clearance of only 3 μm to the probe base and ensures the probe alignment within a stacking plane. By positioning the probes in the recess, a flat surface for the parallel stacking of the electrode arrays is also provided. Dedicated alignment structures implemented as interlocking pins and shallow recesses, in the following referred to as receptacles, further limit in-plane translational as well as rotational shifts among multiple SEAs during stacking (figures 1(d) and 2). Four receptacles are located on the front side (FS) of a stacking module, while four pins occupy corresponding positions on the rear side (RS). The two larger split pins and receptacles feature in addition through-holes in their centers, which

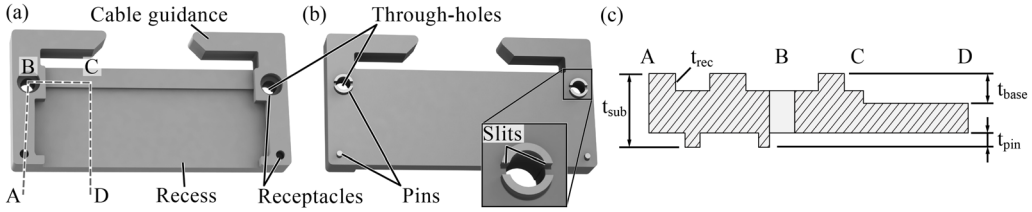

Figure 2. Schematic of the stacking module: perspective (a) front and (b) rear view; (c) cross-section along the line ABCD in (a).

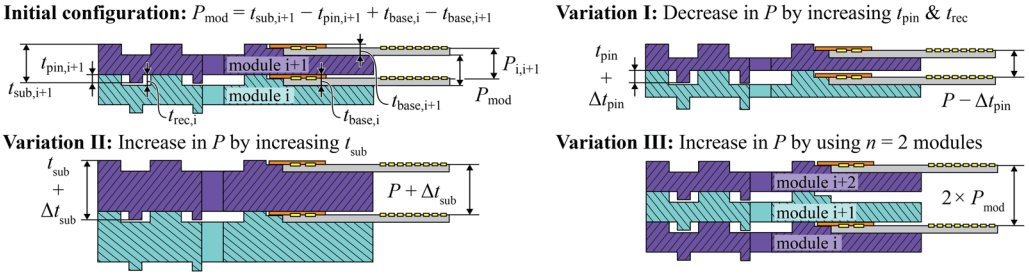

Figure 3. Schematic cross-section of a stack of two SEAs along the line ABCD in figure 2. (a) Stacking modules are fabricated from substrates with thickness t_{sub} and have a pin height t_{pin}. The vertical electrode pitch P can be decreased by changing the pin height t_{pin} by Δt_{pin} (Variation I) or increased by changing t_{sub} by Δt_{sub} (Variation II). Introducing an additional stacking module increases P by P_{mod} (Variation III).

support the distribution of adhesive during probe assembly (see section 2.3) (figure 2(c)).

An important feature of the stacking approach described here is the flexible definition of the vertical separation distance between the planes of the stacked electrodes. This so-called vertical electrode pitch is defined by the out-of-plane stacking module dimensions realized using a dedicated fabrication process. The process allows to vary these dimensions over a wide range with μm accuracy by only adapting processing parameters. The features of the stacking modules are created by deep reactive ion etching (DRIE) of Si and a set of complementary etching masks. The vertical electrode pitch is a direct result of this topography illustrated in figure 2(c). While the lateral dimensions are rigidly defined by photolithography, the vertical dimensions are set flexibly by the etching process. The vertical dimensions relevant to the 3D stacking are the depth t_{base} of the probe base recess on the FS of the stacking module, the height t_{pin} of the pins on its RS, and the module thickness t_{sub} (figure 2(c)). The modules inherit their thickness t_{sub} from the Si substrate used for their fabrication. During processing this dimension is preserved. In contrast, the pin height and receptacle depth are controlled during fabrication.

Figure 3 shows a schematic cross-section of two SEAs along the cut ABCD in figure 2(a). It illustrates the vertical stacking period P_{mod} when identical modules are being stacked, and possibilities to vary this period. In case the length of the alignment pins of the upper stacking module $i + 1$ in the initial configuration in figure 3 is shorter than the depth $t_{rec,i}$ of the receptacles of the subjacent module i ($t_{pin,i+1} < t_{rec,i}$), one has $P_{mod} = t_{sub,i+1} - t_{pin,i+1} + t_{base,i} - t_{base,i+1}$. If the etch depths and the substrate thickness are distributed statistically around their respective mean values $\mu(t_{base})$, $\mu(t_{pin})$, and $\mu(t_{sub})$, P_{mod} will likewise be distributed around its mean value $\mu(P_{mod})$, given by

$$\mu(P_{mod}) = \mu(t_{sub}) - \mu(t_{pin}). \quad (1)$$

If in contrast the condition $t_{pin,i+1} > t_{rec,i}$ applies, the stacking period is given by $P_{mod} = t_{sub,i+1} - t_{rec,i} + t_{base,i} - t_{base,i+1}$ and, as a result, one has

$$\mu(P_{mod}) = \mu(t_{sub}) - \mu(t_{rec}). \quad (2)$$

Throughout this study, the condition $t_{pin,i+1} < t_{rec,i}$ is fulfilled, so that equation (1) rather than equation (2) applies.

The most important dimension of the stacked probes is the vertical electrode pitch P. For a given module variant, P depends on P_{mod} and the number n of stacking modules between two considered electrode planes i and $i + n$, so that

$$\mu(P_{i,i+n}) = n\mu(P_{mod}). \quad (3)$$

Three options exist for the modification of P: (i) adjusting the etch depths t_{pin} and t_{rec}, (ii) varying the substrate thickness t_{sub} and (iii) increasing the number n of stacking modules, as shown in figure 3. In Variation I, the pitch P was altered by increasing the RS etch depth. This requires the FS etch depth to be adjusted as well such that the alignment pins fit into the corresponding receptacles. Alternatively, an increase of t_{sub} leads to a corresponding increase in P, as shown by Variation II. Virtually any pitch smaller than the thickness of common Si substrates (e.g. for standard 300, 380 and 525 μm thick wafers) can thus be implemented. The third variation is the insertion of empty stacking modules between two SEAs to increase P in integer steps of P_{mod}. However, variations in t_{sub} or in the etch depths are reflected in the uncertainty of P_{mod} and P. Using the standard deviation (Std Dev) σ of the various design dimensions as a measure of their uncertainty, the following equation applies

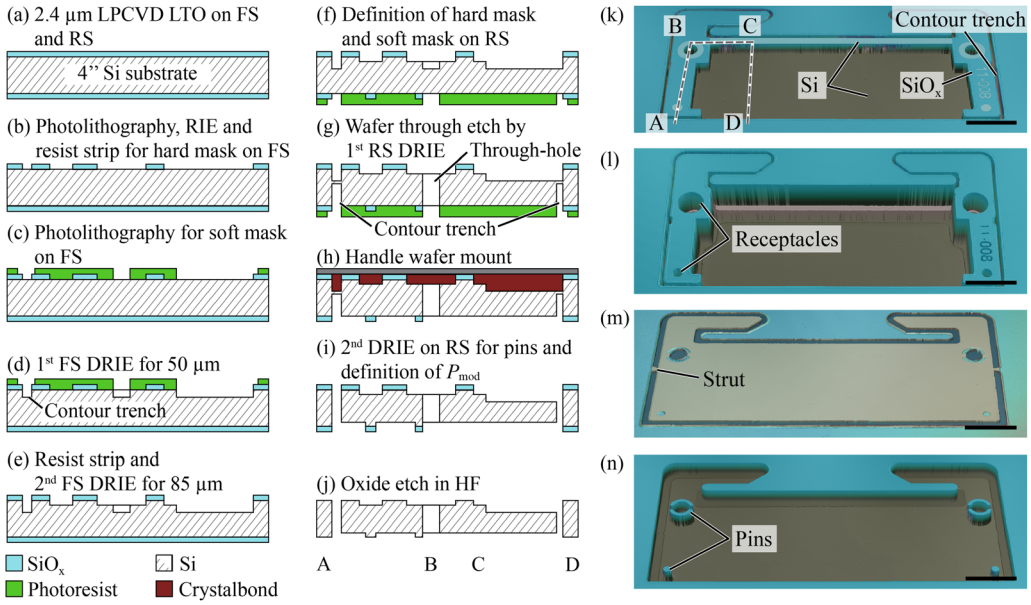

Figure 4. (a)–(j) Microfabrication scheme of the stacking modules applying DRIE from the wafer (a)–(e) FS and (f)–(i) RS; (k)–(n) exemplary surface profiles recorded after respective DRIE steps using white light interferometry; scale bars are 500 μm.

$$\sigma^2(P_{\text{mod}}) = \sigma^2(t_{\text{sub},i+1} - t_{\text{pin},i+1} + t_{\text{base},i} - t_{\text{base},i+1}).$$

We assume that the individual geometric dimensions are uncorrelated. As the process steps responsible for these dimensions do not affect each other, this assumption can safely be made. As a results, the variance of P_{mod} is obtained as

$$\sigma^2(P_{\text{mod}}) = \sigma^2(t_{\text{sub}}) + \sigma^2(t_{\text{pin}}) + 2\,\sigma^2(t_{\text{base}}). \quad (4)$$

In case of P of probes separated by n stacking modules, it is also necessary to account for variations in the probe thickness t_{pr}, which translates into

$$\sigma^2(P_{i,i+n}) = n(\sigma^2(t_{\text{sub}}) + \sigma^2(t_{\text{pin}})) + 2\,\sigma^2(t_{\text{base}}) + 2\,\sigma^2(t_{\text{pr}}). \quad (5)$$

Whether the magnitude of the deviations is uncritical for a given applications in neuroscience needs to be assessed case by case. In section 3, we present a detailed characterization of the accuracy of our fabrication and assembly approach.

2.2. Microfabrication

As illustrated in figure 4, DRIE on the FS and RS of 4" double-side polished Si substrates is used to realize the stepped topography of the stacking modules illustrated in figure 2(c). A combination of photoresist and silicon oxide (SiO_x) used as etch mask layers enables a sequential pattern transfer with the required lateral and vertical resolution.

The fabrication process starts with determining the wafer thickness t_{sub} at 11 positions across the wafer surface. The step is required for defining the stacking period P_{mod} by adjusting the RS etch depth t_{pin} according to the actual substrate thickness. For this study, we used prime grade silicon substrates (Okmetic Oyj, Vantaa, Finland) with nominal thicknesses of 300 and 380 μm. The thickness measurement is followed by the low-pressure chemical vapor deposition (LPCVD) of 2.4-μm-thick silicon oxide layers on both sides of the wafers (figure 4(a)). Next, the oxide on the wafer FS is patterned by means of photolithography and reactive ion etching (RIE) to define the outline of the stacking module and the probe base recess. Following the removal of the photoresist (PR) layer (figure 4(b)), the SiO_x hard mask is partially covered with a PR soft mask (figure 4(c)). This PR mask is used in the first DRIE step which transfers the contour of the stacking modules and the probe base recess into the Si wafer (figure 4(d)). The resulting wafer topography recorded by white light interferometry (WLI) is shown in figure 4(k). Removal of the PR mask exposes the complete silicon oxide mask for the second FS DRIE step used to define the receptacle structures and deepen the probe recess and module contour (figure 4(e)). The cumulative nominal etch depth for the probe recess and contour trench is 135 μm. This recess depth was chosen to accommodate up to 100 μm thick electrode arrays comprising ribbon cables with a thickness of roughly 10 μm. The corresponding WLI profile after the second FS DRIE step is shown in figure 4(l).

The RS of the wafers is then processed similarly with adapted etch depths. In the first RS DRIE step, the stacking module contour is almost etched through the wafer (figure 4(g)). At this point the wafer-through etching of the large circular holes has already been completed, due to the aspect-ratio dependence of the etch rate. The contour is finished in the second RS DRIE step. Therefore, the substrates are mounted to handle wafers using a thin layer of a water-soluble wafer mount adhesive (Crystalbond 555HMP, Aremco Products Inc., Valley Cottage, NY, USA) (figure 4(h)). Struts integrated on the short sides of the stacking modules secure the components inside the fabrication wafers during the final process steps (figure 4(m)). The final RS DRIE step defines the height t_{pin} of the alignment pins on the RS of the modules and the stacking period P_{mod} (figure 4(i)). The respective WLI profile after the RS DRIE is shown in figure 4(n). The SiO_x masking layers on the FS and RS are finally removed using hydrofluoric acid

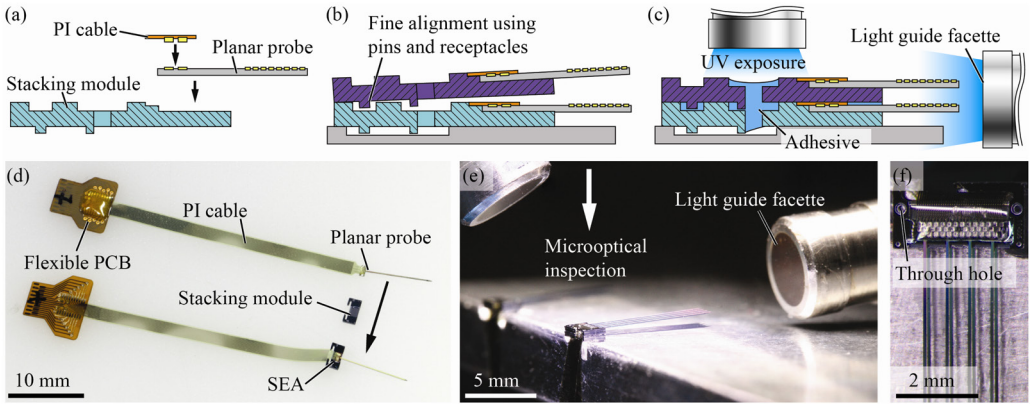

Figure 5. Assembly sequence of 3D electrode arrays; (a)–(c) schematic representation showing (a) assembly of a SEA, (b) stacking and fine alignment of multiple SEAs, and (c) adhesive bonding of the SEA stack. Photographs of (d) planar probe and stacking module at different stages during SEA assembly and (e) probes in assembly jig with light guide setup for fine alignment and adhesive bonding. (f) Optical micrograph showing top view of a SEA in the assembly jig.

(HF) (figure 4(j)). Following the oxide removal, the depth t_{base} of the probe base recess and the pin height t_{pin} are measured using WLI at the same 11 positions as used for the substrate thickness determination.

The fabrication of the Si-based electrode arrays and the interfacing PI ribbon cables follows established procedures of our group [27, 28]. Single-shank and comb-shaped electrode arrays with thicknesses of 50 and 100 μm and up to 32 sputter-deposited platinum (Pt) electrodes are used in this work. They are fabricated from standard Si substrates using DRIE to create the outline of the probe array and RS grinding to define the probe thickness [28]. The highly flexible PI cables are 10 μm thick, 30 mm long and equipped with electroplated gold bumps. The bonding bumps enable the electrical and mechanical connection to the electrode arrays and fPCBs using flip-chip (FC) bonding and soldering, respectively [27].

2.3. 3D assembly

The assembly of the 3D probe array is schematically outlined in figures 5(a)–(c). In a first step, fPCBs are connected to the PI cables for interfacing the individual probes of the 3D array during neural recording. The cables are soldered to the fPCBs, with the solder pads subsequently covered by a biocompatible glob-top (EPO-TEK 353ND-T, Epoxy Technology Inc., Billerica, MA, USA). The fPCBs fit into zero-insertion-force (ZIF) connectors (FFC-FPC SMT Connector 0.25 mm Pitch Easy-On, MOLEX, Lisle, IL, USA). Next, electrode arrays are connected to the PI cables in an ultrasound-assisted FC bonding process (figure 5(a)) followed by an electrical functionality test of the individual planar probes. The planar probe is then manually positioned inside the stacking module recess and aligned against the distal sidewalls with the help of tweezers under optical inspection using a stereo microscope. The probe base is fixed inside the stacking module using a UV light- and heat-curable, medical grade adhesive (1128A-M Multi-Cure, Dymax Europe GmbH, Wiesbaden, Germany). The adhesive is certified for implantation according to ISO10993 and its stability was characterized by the manufacturer using accelerated aging at 60 °C and 55% relative humidity for up to 56 d [29]. The thorough curing of the adhesive in the shadowed areas next to and underneath the probe base is ensured in a subsequent thermal curing step at 110 °C. Photographs of the array components at different stages of assembly are shown in figure 5(d). Next, multiple SEAs are coarsely aligned to each other by bundling all cables and threading them into the guidance structures of the stacking modules. The pre-aligned stack is transferred into an assembly jig for fine alignment and adhesive bonding (figure 5(b)). The built-in alignment structures, i.e. receptacles and pins, are then used for the in-plane fine alignment of different SEA relative to each other. As soon as the pins and receptacles interlock, the stack is adhesively bonded using the dual-curing adhesive (figures 5(c) and (e)). The adhesive is dispensed into the through-holes in the topmost stacking module (figure 5(f)). It flows through the stack and spreads sideways through the pin slits into the cavities between the stacked modules. The plasma-etched surface on the RS of the modules facilitates the extended spreading of the adhesive between the modules by capillary forces. UV exposure then bonds the modules sufficiently strongly so that the stack can be transferred into an oven for the final thermal curing.

Using this assembly scheme, additional test structures were prepared to characterize the alignment of individual probes within a 3D probe array (figure 6). The optical test sequence applies WLI from two orthogonal directions, as indicated in figure 6(a). The first WLI measurement records the topography of the test structures from the FS of the assembled stack to extract the vertical electrode pitch and the angular off-orientation θ_{out} in the directions perpendicular to the plane of electrodes (figure 6(b)). In the second step, the profile is recorded from the side and the tilt θ_{in} of the probe shanks parallel to the electrode planes can be measured (figure 6(c)). For these tests, bare Si probe combs were fabricated from ultra-thin Si wafers. These probe combs feature no FS passivation or ground RS surface, thus avoiding any source of fabrication related mechanical stress that may bend the probe shanks [28, 30].

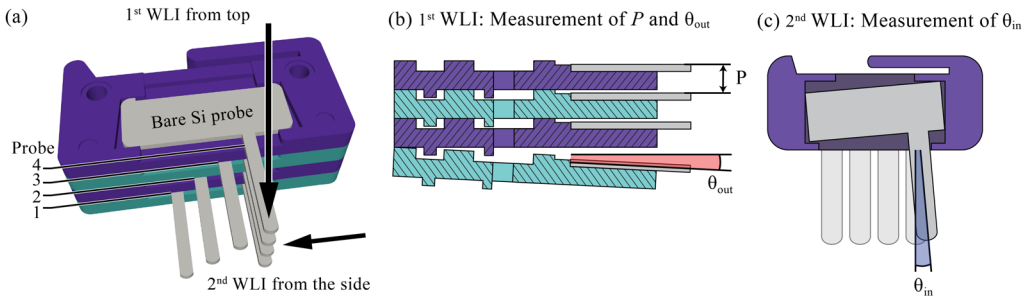

Figure 6. Test structure for the characterization of probe alignment; (a) 3D model of test structures composed of four stacking modules and four bare Si probes with one or two shafts. Subsequent topography measurements of the 3D test probe from top and side used to extract (b) the actual vertical electrode pitch P and out-of-plane tilt θ_{out} and (c) in-plane tilt θ_{in}, respectively.

2.4. Neurophysiological recording methods

The recordings were performed on two male macaque monkeys (*Macaca mulatta*), which will be referred to as M1 and M2. Before starting the recordings, the monkeys were habituated to sit in a primate chair and to interact with the experimenters. Then, a head fixation system was implanted (see below for details on section 2.4.1), and the animals were trained to perform a set of behavioral tasks described in detail in previous papers [31, 32], with the head fixed and using the hand contralateral to the hemisphere to be recorded. When the training was completed, 64-channel 3D electrode arrays were implanted in the pre-supplementary motor area F6 [33] (probe P1 in the left hemisphere of M1 and the probes P2 and P3 in the right hemisphere of M2).

2.4.1. Surgical procedures. All surgeries were performed under general anesthesia (ketamine hydrochloride, 5 mg kg^{-1} intramuscular (i.m.) and medetomidine hydrochloride, 0.1 mg kg^{-1} i.m., repeatedly administered during the surgery). Dexamethasone and prophylactic broad-spectrum antibiotics were administered pre- and postoperatively. Furthermore, analgesics were administered intra- and postoperatively. Dexamethasone administration was continued for 1 week after probe implantation. During all surgeries, hydration of the monkeys was maintained with continuous infusion of saline solution. A heating pad stabilized the body temperature throughout the surgical procedure. The heart rate, respiratory depth and body temperature were continuously monitored. Upon recovery from anesthesia, the animals were returned to their home cages and closely monitored. All experimental protocols complied with the European law on the humane care and use of laboratory animals (directives 86/609/EEC, 2003/65/CE, and 2010/63/EU). They were authorized by the Italian Ministry of Health (D.M. 294/2012-C, 11/12/2012), and approved by the Veterinarian Animal Care and Use Committee of the University of Parma (Prot. 78/12 17/07/2012).

More specifically, for the implantation of the probes the animal was placed in a stereotaxic apparatus, and the skull was trephined over the region of interest to perform a relatively small craniotomy (approximately 10×6 mm). Two self-tap bone screws where then fixed to the skull close to the craniotomy. The dura was then opened and removed, and the probe inserted along the mesial cortical wall. DuraGen (Integra LifeSciences, Plainsboro, NJ) stripes were placed on both sides of the implanted probe in order to replace the explanted dura. A layer of 3–4 mm of dental cement is then applied, in order to seal the craniotomy and probe bases, and to provide stability to the implant by fixing the stack to the adjacent self-tap bone screws. A plastic recording chamber was then fixed to the skull by means of additional bone screws and dental cement, in order to contain and protect the ribbon cables and ZIF connectors interfacing the implanted probes.

At the end of the experiments, M1 was deeply anesthetized with an overdose of sodium thiopental and perfused consecutively with saline, 3.5–4% paraformaldehyde, and 5% glycerol prepared in 0.1 M phosphate buffer through the left cardiac ventricle. The brain was then processed histologically with well-established methodologies to provide evidence of the amount of tissue damage produced by the probe shafts by means of Nissl staining (see [34] for more details on the histological processing).

2.4.2. Recording techniques. Both monkeys were trained to perform the behavioral tasks described in detail in previous works [31, 32]. The main task implied to grasp and pull visually presented objects, namely, a ring, a small cone and big cone, each of which could be grasped with a specific type of grip, i.e. hook grip, precision grip, and power grip, respectively. The monkey had to perform the task with the hand contralateral to the recorded hemisphere. Distinct contact sensitive devices (Crist Instruments, Hagerstown, MD, USA) were used to detect the time of occurrence of the behavioral events of interest, in particular the detachment of the monkey's hand from the starting position and the object pulling onset. Each of these devices provided a TTL signal, which was used by a LabView-based software to monitor the monkey's performance. Eye movement was monitored by means of an eye tracking system composed of a 50 Hz infrared sensitive CCD video camera (Ganz, F11CH4, Cary, NC, USA) and two spots of infrared light, which allowed us to ensure that the animal maintained fixation on the target for the entire duration of the trial. Each correctly performed trial was automatically rewarded with a drop of juice with a dedicated, computer-controlled reward delivery system (Crist Instruments, Hagerstown, MD, USA).

Each of the implanted 3D electrode arrays comprised two planar probes with four shanks per probe. The shanks had pointy tips, as provided by ATLAS Neuroengineering (Leuven, Belgium), to facilitate probe insertion. The probe

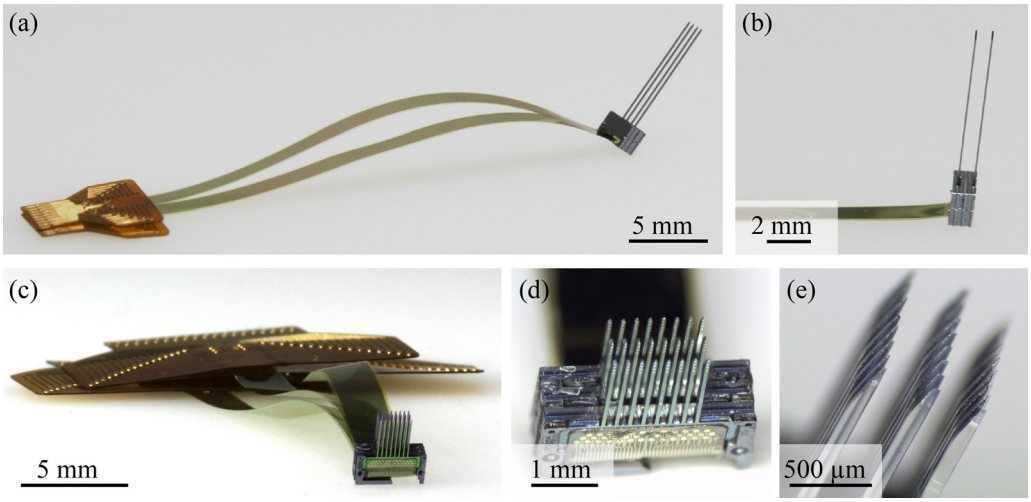

Figure 7. Photographs and optical micrographs of assembled 3D probes; (a) and (b) 64-channel, four-shank probe with 700 μm vertical electrode pitch; (c)–(e) 96-channel, 24-shank probe with 350 μm vertical electrode pitch and (e) pointy-tips. © 2014 IEEE. Reprinted, with permission, from [36].

shanks were 8 mm in length at a width and thickness of 80 μm and 100 μm, respectively. Within the stacking plane, the shanks were separated by 550 μm. The nominal vertical pitch between two stacked 2D electrode arrays was set to 350 μm. A linear array of eight Pt recording sites with an inter-electrode spacing of 500 μm was located close to the shank tips. They measured 35 μm in diameter and featured at 1 kHz an impedance of around 600 kΩ.

The recordings were carried out by means of a 16-channel Omniplex system (Plexon Inc, Dallas, TX, USA). Since we typically implanted a larger number of channels (up to 128 in case of M2), we tested them in separate blocks of 16 channels per session. The wide band neuronal signals were amplified and digitized at 16 bit resolution, sampled at 40 kHz, and stored in parallel with the main behavioral events and the digital signals related to the task stages. All quantitative analyses of neuronal data were performed offline, by means of dedicated software, with conventional methodologies (see [13]).

During the first days of recording, neuronal activity from each set of 16-channels was collected when the monkey performed the behavioral tasks: the results obtained from the detailed analysis of these data is presented in a distinct paper [35]. In addition, neuronal activity was sampled from each set of 16 channels about 2 d per week, for 1 min and across 42 d, while the monkey was quietly sitting on the primate chair and when it performed four reaching-grasping acts: this allowed us to collect comparable samples of neural activity in order to monitor the quality of the recording of the chronically implanted probes over time. After 42 d post-implantation, intracortical microstimulation (ICMS) was performed with the implanted probes (P2 and P3) in the framework of another experiment [35]. Although some electrodes continued to detect good quality single-unit activity for several months, ICMS did impact on the quality of the neural recordings carried out immediately afterwards in most electrodes. Therefore, the systematic monitoring of neural activity was stopped at this point.

2.4.3. Data analyses. Single-unit activity was isolated using standard principal component and template matching techniques, provided by dedicated offline sorting software (Plexon Inc.), as previously described elsewhere (see [13]). Neuron discharge has been statistically analyzed in order to identify neuronal response properties, as described in previous studies based on the same behavioral task [31]. In cases where single units could not be detected using conventional criteria [13], possible significant modulations of the whole multi-unit activity during the various epochs of a task were assessed by considering all the waveforms exceeding the threshold (after artifacts removal) aligned to the visual presentation of the target object or to the object pulling onset.

In order to assess the stability of single cell isolation over time, 1 min recordings were taken for approximately two times per week from all channels, over a period of 42 d. The 1 min recordings collected all along this period were merged together and analyzed offline as a single file. In this procedure, the same threshold amplitude for spike detection and parameters/operations for spike sorting were applied to each channel over the entire recording period.

3. Results and discussion

3.1. Fabrication and probe assembly

We fabricated stacking modules with nominal stacking periods of 250, 300 and 350 μm to implement assembly test structures for characterization purposes as well as functional recording probes. Figure 7 shows exemplary fabrication and assembly results that reflect the versatility of this prototyping approach. The probe shown in figures 7(a) and (b) exhibits 64 microelectrodes on 7-mm-long probe shanks and a vertical electrode pitch of 700 μm. A highly dense 3D array is shown in figures 7(c)–(e). The probe features 96 channels, 24 shanks with a length of 2 mm and pointy tip repeated at a vertical pitch of 350 μm. Further, we assembled three probes for the *in vivo* experiments in macaque monkeys described in section 2.4.2.

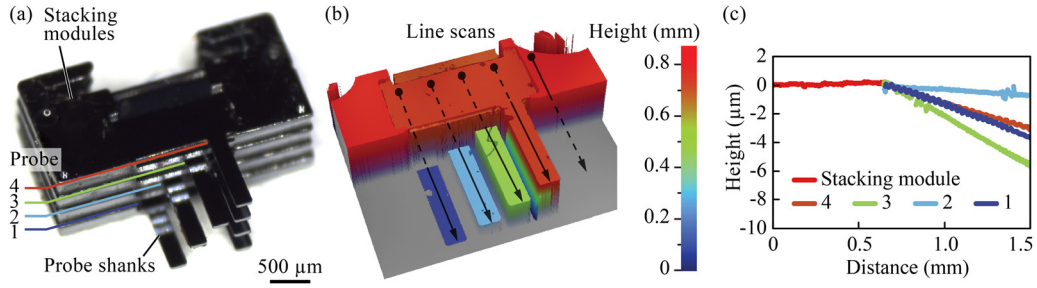

Figure 8. Characterization of probe alignment in the 3D electrode array. (a) Micrograph showing test structure with four bare Si probes numbered in the stacking order. (b) Topography of the probe obtained by WLI measurement from the top. Individual line scans are indicated; dashed lines represent suppressed data points. (c) Exemplary line scan extracted from WLI data in (b); the data of the bare Si probes was truncated at the probe base and the offset (electrode pitch) removed to show out-of-plane tilting of the probe shanks.

The assembly test structures are composed of four bare Si probes assembled at a stacking period of 250 μm. Four samples were assembled, offering 12 measurement points for the actual vertical electrode pitch and 16 measurement points for each of the tilt angles (see section 2.3).

3.1.1. Module fabrication. Directly after the last fabrication step, the stacking period was extracted by measuring the topography of the devices and calculating the mean and variance of the stacking period P_{mod}, as stated in equations (1) and (4), using the substrate thickness t_{sub} and the depths of the FS and RS DRIE etch steps, i.e. t_{base} and t_{pin}, respectively. The achievable accuracy of P_{mod} affects (i) the smallest vertical distance between stacked electrode layers that can be implemented and (ii) the smallest, reasonable step size in P_{mod}. Table 1 lists mean values and Std Devs for the measured and predicted dimensions. The three different target values for P_{mod} were realized with very high accuracy, with an offset from the intended values of only about 1 μm.

The Std Dev is similar for all three variants of the stacking module. Its magnitude is predominantly affected by the inhomogeneity of the DRIE process on both the wafer FS and RS. As expected, the impact of the FS etch is related to the weighting factor 2 in equation (4). Due to the fact that the variation of the etch depth scales with the total etch depth, the comparably deep FS etch is most critical for the variation of the stacking period P_{mod}. Still, the Std Dev is smaller than 2% of the mean for the three module variants.

3.1.2. Assembly of stacked probes. The dedicated assembly test structures composed of stacking modules with $P_{\mathrm{mod}} = 250$ μm and bare Si probe combs are shown in figure 8. These probe combs are on average 51.5 μm thick with a Std Dev of 5.5 μm ($n = 12$). For the two tilt angles θ_{in} and θ_{out}, the top-most stacking module was chosen as the reference. Exemplary measurement results for the out-of-plane tilt are shown in figure 8(c). A summary of the measurement results is given in table 2. The mean of P is larger by roughly 9 μm than expected from the fabrication results for P_{mod}. We attribute this to artifacts on the rear side of the stacking modules that originate from unintentional masking and other defects generated during DRIE. Furthermore, the adhesive layer between individual modules certainly affects

Table 1. Measurement data for the substrate thickness t_{sub}, RS and FS etch depth t_{pin} and t_{base}, and the resulting stacking period P_{mod}.

Nominal P_{mod} (μm)	Parameter	Mean (μm)	St Dev (μm)
250	t_{sub}	294.3	0.9
	t_{pin}	45.3	1.4
	t_{base}	139.1	3.2
	P_{mod}	248.9	4.8
300	t_{sub}	376.4	0.6
	t_{pin}	74.8	1.6
	t_{base}	141.2	2.2
	P_{mod}	301.5	3.6
350	t_{sub}	375.6	0.6
	t_{pin}	26.5	0.7
	t_{base}	141.8	2.2
	P_{mod}	349.1	3.2

Table 2. Probe pitch and shank tilt of stacked probes with a nominal pitch of 250 μm.

	Mean	Std Dev	Samples
P (μm)	257.9	10.7	12
θ_{out} (°)	0.01	0.32	16
θ_{in} (°)	0.11	0.29	15

P, as well. The Std Dev is also increased compared to that of the stacking modules. Based on equation (5) and the variance of the probe thickness, the expected Std Dev of P is 9.1 μm. This is comparable to the measured Std Dev of P and explains the increase of around 5 μm compared to the Std Dev of P_{mod}.

Tilting of the probe shanks was found to be very low in both the in-plane as well as out-of-plane directions. On average, both angles θ_{in} and θ_{out} are almost 0° with a Std Dev of around 0.3° indicating no pronounced, systematic tilt in any direction. This supports the impression that the probe shanks are extremely well aligned in our assembly approach.

3.2. Neurophysiological results

We tested three probes of identical design (see section 2.4.2), labelled as P1, P2 and P3, in two awake behaving macaque monkeys (M1 and M2). We performed a preliminary implantation test of P1 in M1 (which was used for previous

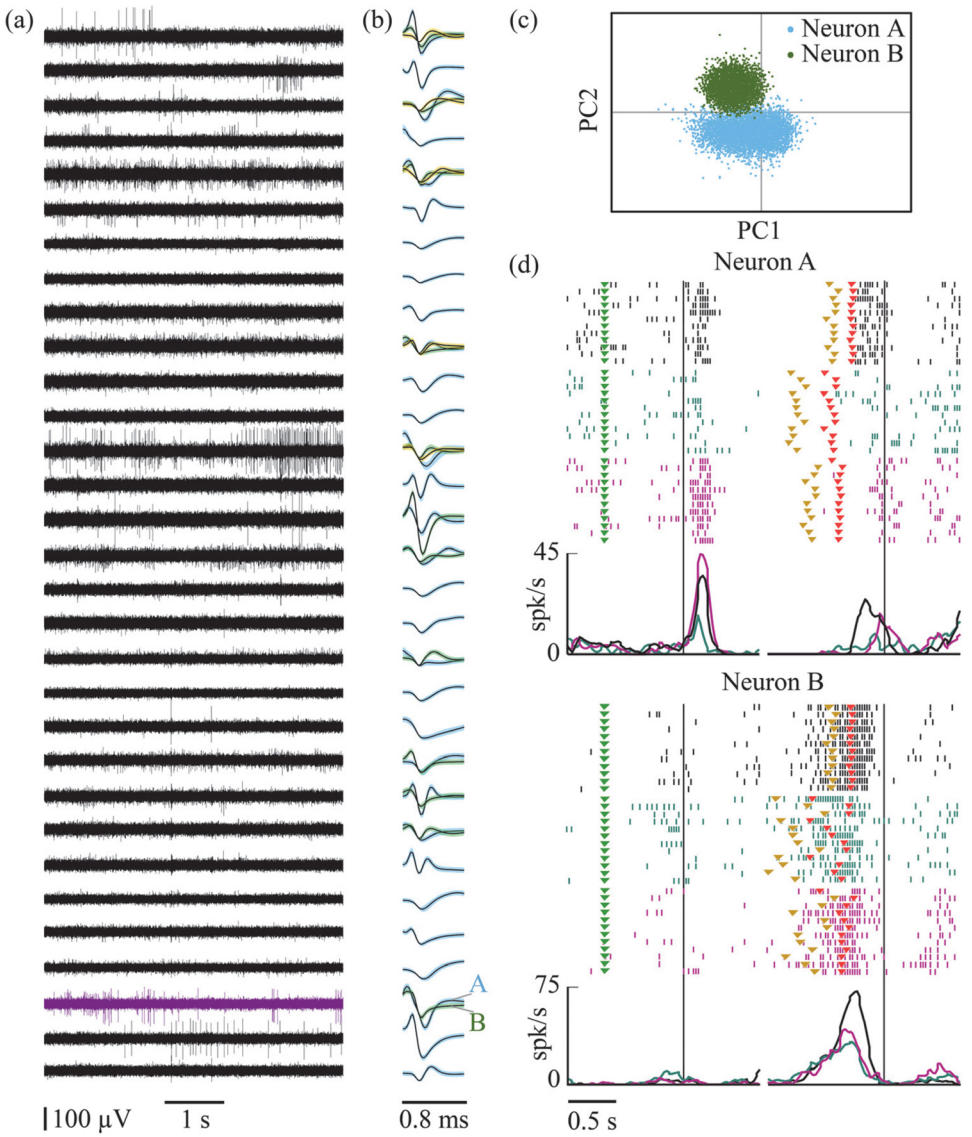

Figure 9. Neuronal recordings obtained with probe P1 in the left pre-supplementary motor area F6 of M1; (a) 5 s samples of filtered neuronal signals (300–7000 Hz) of the 31 channels showing SUA. The channel highlighted in purple includes the neurons whose activity is shown in panels (c) and (d). (b) Sorted waveforms recorded from each of the channels shown in (a). (c) 2D PCA of the spikes attributed to the neurons labeled as A and B in panel (b), simultaneously recorded from the same channel (shown in purple in (a)). Note that spike sorting has been performed using PC3 as well to ensure a better separation of spikes generated by different neurons. (d) Functional properties of neurons A and B during the behavioral grasping task. The rasters show spiking activity during 12 trials for each of the three tested target objects: ring (black), small cone (green) and big cone (purple). Peri-event spike density function and rasters are aligned (vertical solid lines) to object presentation during go-trials (left) and object pulling onset (right, after the gap). Colored triangular markers: auditory cue for go-trials (green), go signal (gold), and movement on-set (red).

experiments and had to be sacrificed a few weeks later) in order to validate the surgical procedure (see section 2), assess the quality of the recorded signal, and evaluate histologically the amount of tissue damage produced by the probe shafts. Probes P2 and P3 were implanted in a second monkey, in order to better evaluate the stability of the recorded signals over a longer period of time.

3.2.1. Recording quality and histological data. Electrode array (P1) was implanted in M1, in the left pre-supplementary motor area F6 [33]. One of the eight shanks broke during handling of the probe, so seven shanks and a total of 56 channels remained available. We recorded from all the available electrodes during the first week following the probe implantation, and obtained significantly modulated activity in 45 out of 56 available channels (see table 3 for details): 31 electrodes showed SUA and 14 only MUA. In total, we could isolate 48 single units from the 31 electrodes with SUA. Figure 9(a) shows 5 s samples of the filtered (300–7000 Hz) signal recorded from all these channels. Figure 9(b) illustrates all the 48 single unit waveforms (±1 Std Dev) isolated from these channels. Figure 9(c) shows a 2D principle components analysis (PCA) of the spikes attributed to the two single neurons, labeled as A and B, recorded from the same

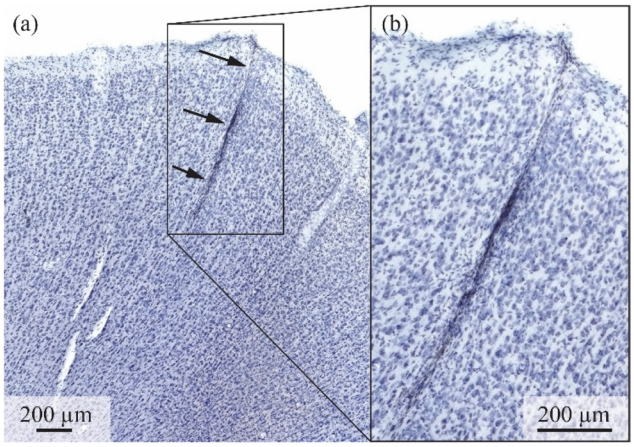

Figure 10. Micrographs of Nissl-stained tissue section obtained from the pre-supplementary motor area F6 in M1; arrows indicate the track formed by a single shaft of the implanted 3D electrode array P1.

channel shown in figure 9(b) (in purple). Their clearly distinct functional properties when the monkey was performing the behavioral task are illustrated in figure 9(d). It is important to note that Neuron A responded vigorously to the visual presentation of the target object (figure 9(d) left panel, before the gap), particularly of the big cone, and had a weaker motor discharge. In contrast, Neuron B showed no visual presentation response and a strong motor discharge in correspondence with the hand movement onset, particularly when the target was the ring.

In M1 we did not monitor the probe recording performance over time. After 52 d from the implantation, M1 was sacrificed, as described in the section 2. Figure 10 shows a micrograph at different magnifications of a Nissl stained section of the M1 brain region in which the 3D probe was implanted. The gliosis created by one of the probe shafts is represented by the denser trace indicated by the black arrows in panel (a) of figure 10. The tissue damage appears to be limited, since the glia scar seems to extend only little beyond the size of the probe (cross-sectional area of the probe shank: $80 \times 100\ \mu m^2$).

3.2.2. Long-term recording quality and stability. In M2, we simultaneously implanted two probes (P2 and P3) in the right pre-supplementary motor area F6, each featuring 64 channels. We recorded from all the available electrodes with the procedure described in the section 2. More specifically, during the first week we collected the data needed to address different scientific questions (which will be the focus of separate papers) while the monkey was performing different behavioral tasks, including the motor task described above. During the first week of recording we obtained significantly modulated activity in 116 out of the 128 channels: 93 channels showed SUA, 23 only MUA. In total, we could isolate 166 single units. Details about the initial recording performance of each probe are given in table 3.

Figure 11(a) shows a 5 s sample of the filtered (300–7000 Hz) signal recorded from all the channels of P2 with SUA. All the 92 single unit waveforms (±1 Std Dev) isolated from these channels are shown in figure 11(b). Figure 11(c) shows

Table 3. Recording performance of each probe during the behavioral tasks carried out in the first week.

	Channels with			Number of single units
	No activity	MUA	SUA	
P1	11	14	31	48
P2	5	13	46	92
P3	7	10	47	74

a 2D PCA of the spikes attributed to the two single neurons, labeled as A and B, recorded from the same channel shown in figure 11(a) (in purple). Their remarkably different functional properties during task performance are illustrated in figure 11(d): Neuron A has a tonic firing rate of about 20 Hz, which strongly increases just before movement onset and then is strongly inhibited during objects grasping and pulling, while Neuron B shows the opposite behavior, decreasing its tonic firing rate of about 20 Hz from the target presentation to movement onset, and then firing vigorously during reaching, grasping and pulling all the three objects. These findings replicate those obtained with P1 and were qualitatively similar to those obtained with P3 as well, although the total number of single units collected with P3 was slightly lower probably due to the implantation site.

In order to explore the long-term recording properties of these probes, we also collected samples of 1 min of activity approximately twice a week over a period of 42 d from the first day after implantation ($N = 12$ recording sessions). We noticed that, in most cases, the channels showing SUA continued to provide clearly isolated SUA over the entire investigated period, but a crucial issue was to establish whether, and to which extent, the *same* wave-forms (putatively, the same single units) could be detected over time from the same channel. As described in the section 2, we addressed this issue by first merging all the 1 min samples ($N = 12$) collected during the 42 d, and then processing the merged files by means of standard spike-sorting procedures, as if it was the result of a single recording session. Figure 12(a) shows the example of two clearly isolated units (Neuron A and B) simultaneously recorded from a single channel of probe P2. In spite of their good separation during the 42 d recording period (figure 12(b)), it is clear that spikes of Neuron A drifted over time in the first two principal component space, becoming increasingly similar to those of Unit B (see figure 12(c)).

Figure 13 shows the normalized activity of all the putative single units isolated in the merged 42 d recordings from P2 and P3, respectively. We have been able to isolate, from the merged sessions, a total of 128 putative single-units from P2 and 68 from P3: out of them, 96 (75%) from P2 and 41 (60%) from P3 did actually show at least one spike during all the 12 recording sessions. It is clear that, although the criteria used to sort spikes from the total number of waveforms exceeding the threshold and to attribute them to a cluster were the same for the whole investigated period (see section 2), this does not allow one to claim that all these putative single neurons remained steadily isolated over such a long period of time. Indeed, different clusters can not only

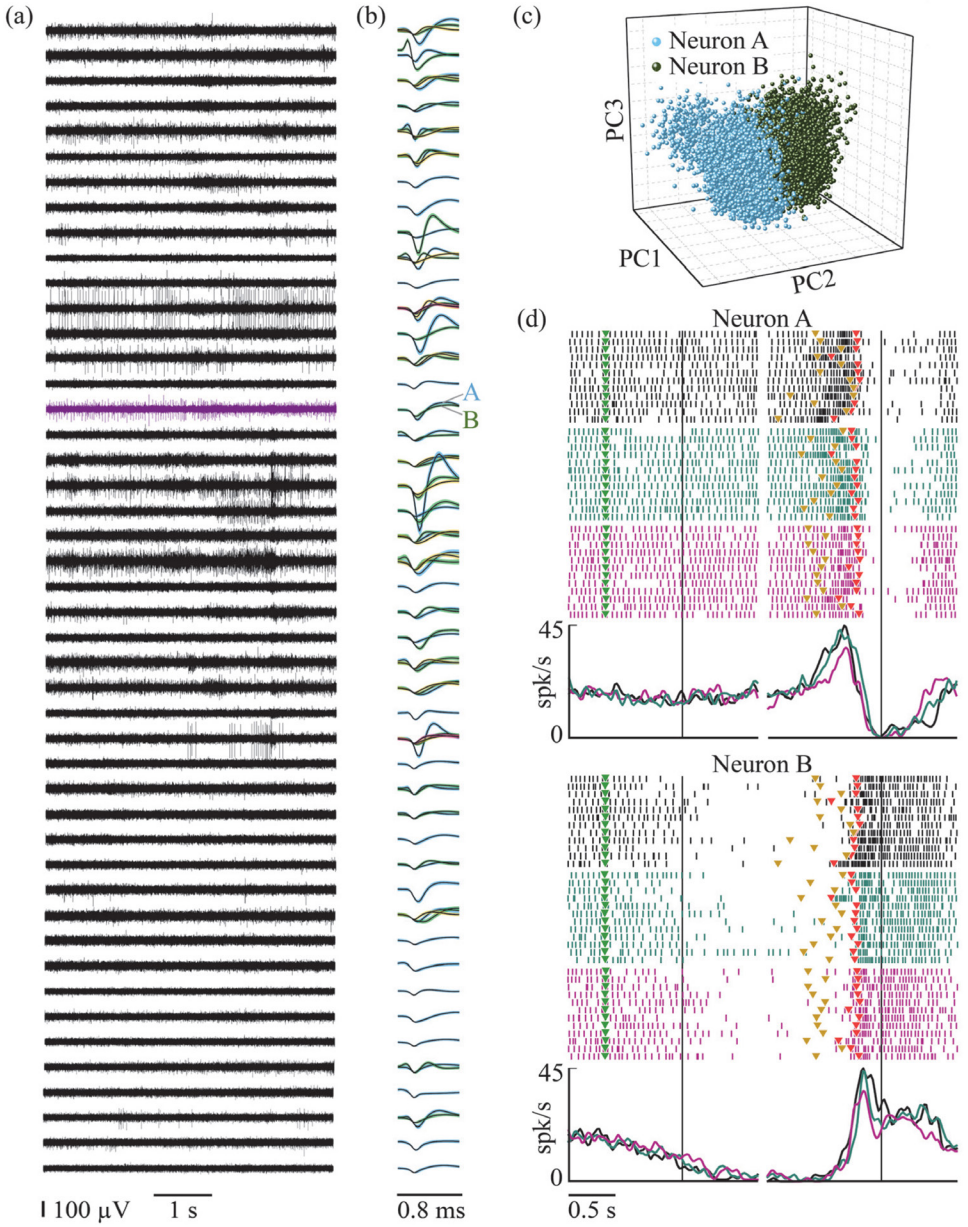

Figure 11. Neuronal recordings obtained with probe P2 in the right pre-supplementary motor area F6 of M2; (a) 5 s samples of filtered raw neuronal signals (300–7000 Hz) of the 46 channels showing SUA. The channel highlighted in purple includes the neurons whose activity is shown in panels (c) and (d). (b) Sorted waveforms recorded from each of the channels shown in (a); (c) 3D PCA of the spikes attributed to the neurons labeled as A and B in panel (b), simultaneously recorded from the same channel (shown in purple in a). (d) Functional properties of neurons A and B during the behavioral task. All conventions as defined in figure 9.

appear or disappear, but can also be detected with variable degree of precision and reliability over time, as shown in figure 12. To provide a quantitative estimation of these variations, we established for each isolated neuron a range of tolerance around its mean activity calculated across all the 1 min sessions, and defined as the mean firing rate over the 12 sessions ±2 Std Dev. Note that since all the sessions were identical in terms of the proportion of resting- and movement-related activity (see section 2), one would expect that if a single neuron remains steadily isolated across sessions, then it should provide a similar level of activity. Our findings show that the firing rate of 59 (46%) neurons from P2 and 41 (35%) neurons from P3 remained within the above defined interval during all the 12 sessions, thus indicating the possibility to achieve a reasonable stability in the isolation of at least some single cells across time.

Although it can be questionable to claim that a single isolated neuron can be reliably detected across several days of recording, it is, however, possible to obtain reasonable evidence of this further possibility by considering multiple criteria. Figures 13(c) and (d) show the exemplary data of a single isolated neuron tested with the behavioral task during Day 1 post-implantation (black). It is clear that a unit with the same spike-shape and functional properties in the behavioral task could be recorded even 42 d later

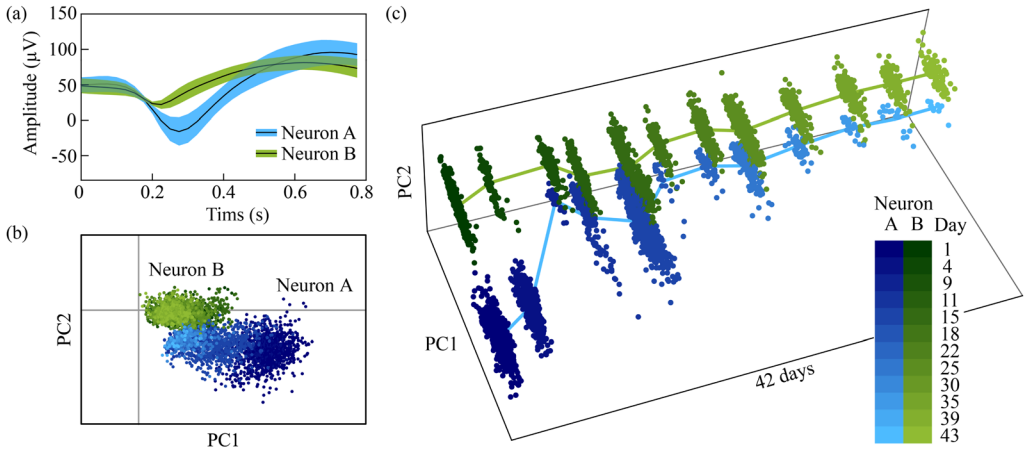

Figure 12. Neuronal data from 12 merged recording sessions (1 min each) covering 42 d from the implantation of probe P2. (a) Waveforms of two putative single neurons (A and B) recorded from a single channel of P2. (b) PCA showing the drift of Neuron A towards Neuron B in the first two principal components space. The drift from Day 1 to Day 43 is evidenced by the shift from dark to light colors, as shown in the legend of panel (c). (c) Time-resolved PCA with solid lines connecting the centroids of each cluster (Neuron A and B) in the 12 recording sessions.

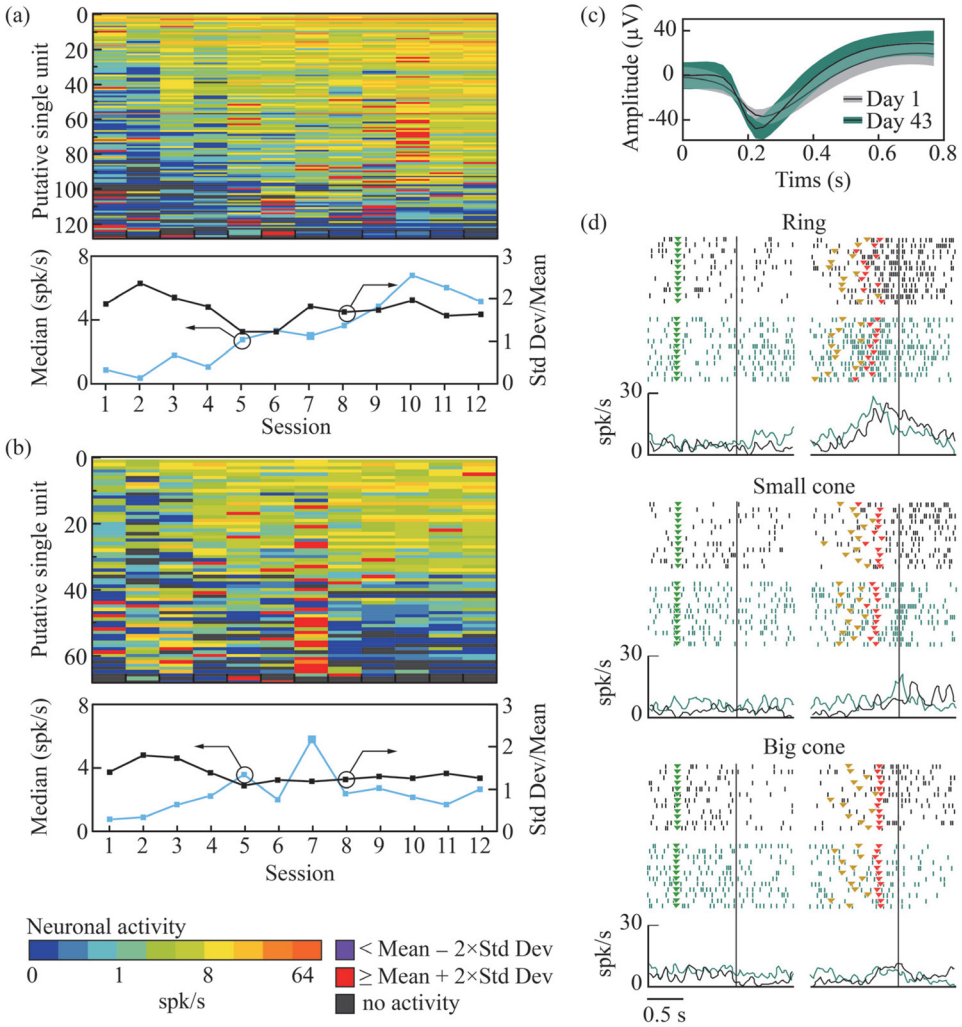

Figure 13. Neuronal activity of (a) 128 putative single units recorded with P2 and (b) 68 putative single units recorded with P3 in the 12 merged recording sessions. The heat maps show the average neuronal activity for each single unit and session. The units are sorted according to the stability of their spiking rate within the 12 sessions (ratio of Std Dev over the mean of the respective neuron's activity in all sessions); higher ranked neurons (on the bottom of each panel) represent the less stable. The graphs summarize the median activity and the ratio of Std Dev over mean of all recorded neurons on each probe for each session. (c) Sorted waveform of the same putative single neuron recorded during Day 1 and Day 43 post-implantation and (d) its functional properties in the motor task tested in Day 1 (black) and Day 43 (green). All other conventions as defined in figure 9(d).

(green) from the same channel. This suggests that the activity recorded during the last day is likely generated by the same single neuron isolated and tested in the first day of recording.

4. Conclusions

This study demonstrated advanced fabrication and assembly procedures for custom-designed neural probes. The described approach offers a high freedom of design and yields accurately defined 3D electrode arrays for neurophysiological experiments. With the micromachined stacking module, a wide range of vertical electrode distances can be realized with an accuracy better than $3.2 \pm 4.2\%$. The fabrication process can be flexibly adjusted to implement a broad range of electrode pitches. There is no need to modify the fabrication tools such as photolithography masks. This enables a pronounced reduction of the lead time for the implementation of new recording prototypes. In addition, the process potentially saves time and money, since variants of stacking modules for distinctly different vertical electrode distances can be processed identically in a single wafer batch until the last etching step. Compared to previous fabrication approaches for 3D electrode arrays, the reported process seems more versatile while offering satisfactory accuracy. In comparison to platform-based probes [15, 16, 20, 21], the system volume is, however, increased due to the modular assembly and the size of the probe bases.

During probe assembly, the concept offers additional freedom in probe design, as demonstrated with 64- and 96-channel probes with four and 24 probe shanks, respectively. Accuracy of the electrode pitch remains high throughout the assembly process. Even more important, the angular misalignment of the probe shanks is well below 1°. This is true both in the plane of the electrodes and in the perpendicular direction. As an example, for arrays with 8-mm-long probe shanks as used in this study, the angular misalignment translates into a $\pm 1\sigma$ spread of the deflection of the tips of less than $\pm 56\ \mu$m. Mechanical loading of the shanks and the size of the lesion caused by insertion are therefore expected to be acceptable.

When relating the number of electrodes in our demonstrated systems to the footprint of the implanted portion of the array, we achieved an electrode density of almost 98 electrodes mm^{-2}. To our knowledge, the highest electrode density demonstrated so far for passive 3D electrode arrays is around 31 electrodes mm^{-2}, again referred to the implanted portion of the array [7]. The electrode density of our arrays could be increased even further; it is currently limited by the planar probes. Multiplexed CMOS probes, for instance, would allow a significant increase in recording site density [37–39].

For the Pt microelectrode arrays used in this study, we observed a standard deviation of the electrode impedances of around 22% of the mean value for individual planar probes. This spread will likely further increase in case of 3D arrays where planar probes from potentially different fabrication runs are combined. Among the recording channels, the impedance variability will cause variations in the signal quality and will likely make it difficult to quantitatively compare signal amplitudes. A solution to this problem would be to use specific post-processes to tune the electrode impedances [40]. Also, the implementation of iridium oxide-based microelectrodes, which show in our own experience a smaller impedance spread, is an option. In the behavioral experiments performed in this study, however, the variability of electrode impedance was not a problem.

We demonstrated the full functionality of the stacked probes and their recording quality *in vivo* with awake behaving monkeys. In the behavioral experiments, SUA was recorded from more than 60% of the channels of three different probes. A typical number reported for the UEA is in the order of 33% [8]. With effectively well over one recorded unit per channel, we were able to gather a large data set to assess the sensorymotor functions of the investigated region. The median of spiking activity across all recorded units and the number of channels with SUA generally increased over the monitored period of time (42 d). In addition, by using multiple modalities, we demonstrated a relatively good stability of neuronal isolation, with some cells showing not only a stable and well-isolated spike shape over the entire recording period but also a constant level of activity and tuning properties in the motor task. These results are in line with a low tissue reaction after 52 d post-implantation (figure 10).

In view of their bio-stability, we expect the probes to be suitable for implantations of several months. For other Si-based probes, stable operation over extended periods has been demonstrated [41, 42]. The stability of the adhesive bond strength was further verified by accelerated aging by the adhesive manufacturer [29]. Even though integral parts of this probe are made of polymers and, thus, do not form a hermetic seal against water vapor, a reliable operation of the device can be expected for several month as long as clean interfaces during fabrication and assembly are provided and a stable bond between the adhesive and the Si-based components is maintained [43, 44]. The layered structure of the stacked probes increases the diffusion paths, which is propitious to a long implant lifetime. However, for long-term implantations of several years, additional protective layers, e.g. Parylene-C [42] or atomic layer deposited (ALD) aluminum oxide [45], and alternative assembly approaches [46] definitely need to be considered.

In this study, the mechanical stability of the implant was supported by encapsulating the probe stack and cables in dental cement (see section 2.4.1). Further, this procedure sealed the craniotomy and provided protection against infections, which represents a mayor prerequisite for long-term recordings in behaving NHP.

In a recent neurophysiological work [35] carried out with the same 3D electrode arrays as used in this study and in an earlier report using similar probes [47], it has been shown that the probe technology can also be used for intracortical electrical microstimulation. This additional functionality further expands the potential versatility of the reported stacking system. Altogether, the results of this paper support the design of application-specific neural interfaces for neuroscientific research and may be a promising option for the development of new neural interfaces for prosthetic applications.

Acknowledgments

The research leading to these results has received partial funding from the BrainLinks-BrainTools Cluster of Excellence funded by the German Research Foundation (DFG, grant number EXC 1086). Neurophysiological experiments have been partially supported by the Italian Institute of Technology, the European Commission grant Cogsystems (FP7-250013) and the European Research Council grant WIRELESS (678307). The authors greatly acknowledge the support from ATLAS Neuroengineering in the processing of the planar microelectrode arrays, and Marzio Gerbella for anatomical and histological processing.

References

[1] Nicolelis M A L 2008 *Methods for Neural Ensemble Recordings* vol 19985764 ed M Nicolelis (Boca Raton, FL: CRC Press) (doi: 10.1201/9781420048254)
[2] Bansal A K, Truccolo W, Vargas-Irwin C E and Donoghue J P 2012 Decoding 3D reach and grasp from hybrid signals in motor and premotor cortices: spikes, multiunit activity, and local field potentials *J. Neurophysiol.* **107** 1337–55
[3] Campbell P K, Jones K E, Huber R J, Horch K W and Normann R A 1991 A silicon-based, three-dimensional neural interface: manufacturing processes for an intracortical electrode array *IEEE Trans. Biomed. Eng.* **38** 758–68
[4] Jones K E, Campbell P K and Normann R A 1992 A glass/silicon composite intracortical electrode array *Ann. Biomed. Eng.* **20** 423–37
[5] Branner A, Stein R B and Normann R A 2001 Selective stimulation of cat sciatic nerve using an array of varying-length microelectrodes *J. Neurophysiol* **85** 1585–94 (PMID: 11287482)
[6] Bhandari R, Negi S, Rieth L, Normann R A and Solzbacher F 2008 A novel method of fabricating convoluted shaped electrode arrays for neural and retinal prostheses *Sensors Actuators* A **145–6** 123–30
[7] Wark H A C *et al* 2013 A new high-density (25 electrodes/mm^2) penetrating microelectrode array for recording and stimulating sub-millimeter neuroanatomical structures *J. Neural Eng.* **10** 45003
[8] Normann R A 2007 Technology insight: future neuroprosthetic therapies for disorders of the nervous system *Nat. Clin. Pract. Neurol.* **3** 444–52
[9] Bouton C E *et al* 2016 Restoring cortical control of functional movement in a human with quadriplegia *Nature* **533** 247–50
[10] Shandhi M M H, Leber M, Hogan A, Bhandari R and Negi S 2015 A novel method of fabricating high channel density neural array for large neuronal mapping *18th Int. Conf. on Solid-State Sensors, Actuators and Microsystems (TRANSDUCERS 2015)* pp 1759–62
[11] Ruther P, Herwik S, Kisban S, Seidl K and Paul O 2010 Recent progress in neural probes using silicon MEMS technology *IEEJ Trans. Electr. Electron. Eng.* **5** 505–15
[12] Alivisatos A P *et al* 2013 Nanotools for neuroscience and brain activity mapping *ACS Nano* **7** 1850–66
[13] Bonini L, Maranesi M, Livi A, Bruni S, Fogassi L, Holzhammer T, Paul O and Ruther P 2014 Application of floating silicon-based linear multielectrode arrays for acute recording of single neuron activity in awake behaving monkeys *Biomed. Eng.* **59** 273–81
[14] Wise K D, Angell J B and Starr A 1970 An integrated-circuit approach to extracellular microelectrodes *IEEE Trans. Biomed. Eng.* **BME-17** 238–47
[15] Perlin G E and Wise K D 2008 A compact architecture for three-dimensional neural microelectrode arrays *30th Annual Int. Conf. of the IEEE Engineering in Medicine and Biology Society* (*EMBS 2008*) pp 5806–9
[16] Aarts A A A, Neves H P, Puers R P and Van Hoof C 2008 An interconnect for out-of-plane assembled biomedical probe arrays *J. Micromech. Microeng.* **18** 1–8
[17] Kisban S, Holzhammer T, Herwik S, Paul O and Ruther P 2010 Novel method for the assembly and electrical contacting of out-of-plane microstructures *IEEE 23rd Int. Conf. on Micro Electro Mechanical Systems (MEMS 2010)* pp 484–7
[18] Herwik S, Holzhammer T, Paul O and Ruther P 2011 Out-of-plane assembly of 3D neural probe arrays using a platform with SU-8-based thermal actuators *16th Int. Solid-State Sensors, Actuators and Microsystems Conf. (TRANSDUCERS 2011)* pp 2323–6
[19] Barz F, Holzhammer T, Paul O and Ruther P 2013 Novel technology for the in-plane to out-of-plane transfer of multiple interconnection lines in 3D neural probes *17th Int. Conf. on Solid-State Sensors, Actuators and Microsystems (Transducers and Eurosensors XXVII)* pp 884–7
[20] Cheng M-Y, Yao L, Tan K L, Lim R, Li P and Chen W 2014 3D probe array integrated with a front-end 100-channel neural recording ASIC *J. Micromech. Microeng.* **24** 125010
[21] Merriam M E, Dehmel S, Srivannavit O, Shore S E and Wise K D 2011 A 3D 160-site microelectrode array for cochlear nucleus mapping *IEEE Trans. Biomed. Eng.* **58** 397–403
[22] 2015 *NeuroNexus Matrix Array* (Ann Arbor: NeuroNexus) http://neuronexus.com/blog/matrix-array (Accessed: 12 July 2016)
[23] Herwik S *et al* 2009 Fabrication technology for silicon-based microprobe arrays used in acute and sub-chronic neural recording *J. Micromech. Microeng.* **19** 74008
[24] Du J, Roukes M L and Masmanidis S C 2009 Dual-side and three-dimensional microelectrode arrays fabricated from ultra-thin silicon substrates *J. Micromech. Microeng.* **19** 75008
[25] Chang C-W and Chiou J-C 2013 A wireless and batteryless microsystem with implantable grid electrode/3-dimensional probe array for ECoG and extracellular neural recording in rats *Sensors* **13** 4624–39
[26] Musallam S, Bak M J, Troyk P R and Andersen R A 2007 A floating metal microelectrode array for chronic implantation *J. Neurosci. Methods* **160** 122–7
[27] Kisban S, Kenntner J, Janssen P, Metzen R V, Herwik S, Bartsch U, Stieglitz T, Paul O and Ruther P 2009 A novel assembly method for silicon-based neural devices *Proc. IFMBE* pp 107–10
[28] Herwik S, Paul O and Ruther P 2011 Ultrathin silicon chips of arbitrary shape by etching before grinding *J. Microelectromech. Syst.* **20** 791–3
[29] 2016 *Multi-Cure 1128A-M* (Torrington: Dymax Corporation) www.dymax.com/index.php/en/adhesives/products/1128a-m (Accessed: 08 December 2016)
[30] Takyu S, Kurosawa T, Shimizu N and Harada S 2006 Novel wafer dicing and chip thinning technologies realizing high chip strength *Proc. 56th IEEE Electronic Components and Technology Conf.* pp 1623–7
[31] Bonini L, Maranesi M, Livi A, Fogassi L and Rizzolatti G 2014 Space-dependent representation of objects and other's action in monkey ventral premotor grasping neurons *J. Neurosci.* **34** 4108–19
[32] Maranesi M, Livi A, Fogassi L, Rizzolatti G and Bonini L 2014 Mirror neuron activation prior to action observation in a predictable context *J. Neurosci.* **34** 14827–32

[33] Matelli M, Luppino G and Rizzolatti G 1991 Architecture of superior and mesial area 6 and the adjacent cingulate cortex in the macaque monkey *J. Comp. Neurol.* **311** 445–62
[34] Belmalih A, Borra E, Contini M, Gerbella M, Rozzi S and Luppino G 2009 Multimodal architectonic subdivision of the rostral part (area F5) of the macaque ventral premotor cortex *J. Comp. Neurol.* **512** 183–217
[35] Lanzilotto M, Livi A, Maranesi M, Gerbella M, Barz F, Ruther P, Fogassi L, Rizzolatti G and Bonini L 2016 Extending the cortical grasping network: pre-supplementary motor neuron activity during vision and grasping of objects *Cereb. Cortex* **26** 4435–49
[36] Barz F, Paul O and Ruther P 2014 Modular assembly concept for 3D neural probe prototypes offering high freedom of design and alignment precision *36th Annual Int. Conf. of the IEEE Engineering in Medicine and Biology Society* (*EMBC 2014*) pp 3977–80
[37] Seidl K, Herwik S, Nurcahyo Y, Torfs T, Keller M, Schuttler M, Neves H, Stieglitz T, Paul O and Ruther P 2009 CMOS-based high-density silicon microprobe array for electronic depth control in neural recording *22nd Int. Conf. on Micro Electro Mechanical Systems* (*MEMS 2009*) pp 232–5
[38] Raducanu B C *et al* 2016 Time multiplexed active neural probe with 678 parallel recording sites *46th European Solid-State Device Research Conf.* (*ESSDERC*) pp 385–8
[39] Fiáth R, Beregszászi P, Horváth D, Wittner L, Aarts A A A, Ruther P, Neves H P, Bokor H, Acsády L and Ulbert I 2016 Large-scale recording of thalamocortical circuits: *in vivo* electrophysiology with the two-dimensional electronic depth control silicon probe *J. Neurophysiol.* **116** 2312–30
[40] Fiáth R, Grand L, Kerekes B, Pongrácz A, Vázsonyi É, Márton G, Battistig G and Ulbert I 2011 A novel multisite silicon probe for laminar neural recordings *Proc. Comput. Sci.* **7** 310–1
[41] Vetter R J, Williams J C, Hetke J F, Nunamaker E A and Kipke D R 2004 Chronic neural recording using silicon-substrate microelectrode arrays implanted in cerebral cortex *IEEE Trans. Biomed. Eng.* **51** 896–904
[42] Suner S, Fellows M R, Vargas-Irwin C, Nakata G K and Donoghue J P 2005 Reliability of signals from a chronically implanted, silicon-based electrode array in non-human primate primary motor cortex *IEEE Trans. Neural Syst. Rehabil. Eng.* **13** 524–41
[43] Donaldson P E K 1996 The essential role played by adhesion in the technology of neurological prostheses *Int. J. Adhes. Adhes.* **16** 105–7
[44] Rubehn B, Bosman C, Oostenveld R, Fries P and Stieglitz T 2009 A MEMS-based flexible multichannel ECoG-electrode array *J. Neural Eng.* **6** 36003
[45] Xie X, Rieth L, Williams L, Negi S, Bhandari R, Caldwell R, Sharma R, Tathireddy P and Solzbacher F 2014 Long-term reliability of Al_2O_3 and Parylene C bilayer encapsulated Utah electrode array based neural interfaces for chronic implantation *J. Neural Eng.* **11** 26016
[46] Ordonez J S, Schuettler M, Ortmanns M and Stieglitz T 2012 A 232-channel retinal vision prosthesis with a miniaturized hermetic package *34th Annual Int. Conf. of the IEEE Engineering in Medicine and Biology Society (EMBC 2012)* pp 2796–9
[47] Calixto R, Salamat B, Rode T, Hartmann T, Volckaerts B, Ruther P, Lenarz T and Lim H H 2013 Investigation of a new electrode array technology for a central auditory prosthesis *PLoS One* **8** 1–6